Biosensors and Bioelectronics: X 31 (2026) 100797

Contents lists available at ScienceDirect

Biosensors and Bioelectronics: X

journal homepage: www.journals.elsevier.com/biosensors-and-bioelectronics-x

Time-resolved monitoring and circuit modeling of trophoblast invasion in a model of human embryo implantation by electric cell-substrate impedance sensing

Dongyang Tang [a], Liubov Izmaylova [b], Anil Can [b], Sven Ingebrandt [a], Rudolf E. Leube [b], Ziyu Gao [a,*]

[a] *Institute of Materials in Electrical Engineering 1 (IWE1), RWTH Aachen University, Aachen, 52074, Germany*
[b] *Institute of Molecular and Cellular Anatomy (MOCA), RWTH Aachen University, Aachen, D-52074, Germany*

ARTICLE INFO

Keywords:
Electric cell-substrate impedance sensing (ECIS)
Trophoblast invasion
Endometrial epithelium
Label-free monitoring
Equivalent electric circuit (EEC)
Invasion dynamics

ABSTRACT

Electric Cell-substrate Impedance Sensing (ECIS) is widely applied as a label-free and non-invasive technology for the *in vitro* monitoring of tissue dynamics through various electrical parameters. Fitting those to circuit models yields insights about cell-substrate and cell-cell interactions. This work reports progress in monitoring complex biological systems with ECIS technology, *i.e.* cell-invasion dynamics, and explores the possibility of quantifying the invasion progress over time.

A human *in vitro* implantation model was utilized, which allowed to examine the interaction between embryonic trophoblast cells and the uterine endometrial epithelium. It involves attachment of the trophoblast to the endometrium followed by invasion. The process was evaluated by monitoring impedance amplitude and phase. Based on cut-off frequencies, quantification of cell resistance and capacitance was achieved by decomposing the impedance spectra to track the invasion process at various time points. To better understand trophoblast invasion dynamics, the *in vitro* equivalent electric circuit (EEC) model from conventional ECIS theory was extended to a three-component model considering the electrode, endometrial monolayer and trophoblast spheroid. Taken together, a multi-step invasion process is proposed: 1) preinvasion - non-contact condition of the spheroidal trophoblast with the endometrial monolayer, 2) early-stage invasion (0-6 h) - trophoblast attachment and endometrial penetration, and 3) late-stage invasion (6-48 h) - spheroid flattening and expansion within the endometrial monolayer.

This work advances the possibility of cell-electrical quantification to monitor biological processes which involve cell and tissue intercalation. This is not only relevant for embryo implantation but also for developmental processes, inflammation and tumor invasion.

1. Introduction

Cell invasion is a process whereby different types of cells intermingle involving cell migration and tissue penetration. It is critically involved in many different events such as endothelial transmigration of inflammatory cells, cellular intercalation during development and metastasis of malignant tumor cells. A similar invasion process occurs during embryo implantation (Classen-Linke et al., 2025; Bentin-Ley et al., 2000; Ruane et al., 2022; Gauster et al., 2022). In this instance, trophoblast cells, which surround the spheroidal embryonic blastocyst circumferentially, attach to the contiguous endometrial epithelium, a one-layered surface tissue lining the entire uterine lumen. The trophoblast cells subsequently penetrate the endometrial epithelium and invade the underlying connective tissue compartment, which provides the nutritive environment for the developing embryo. Implantation failure is a common cause of infertility (Fang et al., 2023; Mao et al., 2017).

Given the fundamental species-dependent differences in implantation and the obvious ethical restrictions on human implantation studies *in vitro* systems are needed to investigate the pathophysiology of human embryo-endometrium crosstalk. To this end, we have developed a co-culture system of human trophoblast-derived AC-1M88 cells and

---

* Corresponding author.
E-mail address: ziyu.gao@iwe1.rwth-aachen.de (Z. Gao).

https://doi.org/10.1016/j.biosx.2026.100797
Received 17 November 2025; Received in revised form 17 May 2026; Accepted 27 May 2026

hormone-sensitive endometrial Ishikawa cells (Sternberg et al., 2024). To mimic the spheroidal embryonal trophoblast-covered blastocysts, we prepare AC-1M88 spheroids that are placed on confluent Ishikawa monolayers. This allows monitoring of trophoblast attachment and their subsequent penetration and invasion of the endometrial monolayer. We have shown that trophoblast adhesion depends on the stiffness of the substrate on which the Ishikawa cells are growing (Sternberg et al., 2024). To study all the multiple factors that may affect trophoblast adhesion and invasion, a high throughput analysis system is much wanted to track the process in quantitative terms.

Optical imaging and magnetic resonance imaging (MRI) techniques were recently developed to probe cell-cell and cell-matrix interaction in spheroid-based models (Wissmann et al., 2025; Kok et al., 2025). As an alternative, Electric Cell-substrate Impedance Sensing (ECIS) has been utilized as a non-invasive and label-free technique, providing a cost-effective and widely applicable possibility for continuous *in vitro* detection of cell dynamics and function (Giaever and Keese, 1984, 1991; Wegener, 2019). Generally, Electrical Impedance Spectroscopy (EIS) is based on perturbing a balanced or steady-state electrochemical system by applying a small sinusoidal signal (voltage or current) over a wide frequency range and monitoring the resulting sinusoidal response (current or voltage) to the applied perturbation (Magar et al., 2021). Applying this technique to cells cultured on metal microelectrodes enables frequency-dependent monitoring of complex biosystems (Wegener et al., 1996; Hazelgrove et al., 2025). The cell structure, electrodes, and the cell culture environment can be represented by passive electrical elements, allowing for the construction of equivalent electrical circuit (EEC) models (Wegener et al., 2000; Jiang et al., 2024; Kauth et al., 2024; Franks et al., 2005). Various commercial systems, such as the ECIS Z-Theta station from Applied BioPhysics (Applied BioPhysicsInc, 2025) and the xCELLigence Real-Time Cell Analysis Analyzer from Agilent (Agilent, 2025) have been developed to monitor time-resolved cellular behaviors through impedance measurement inside an incubator.

In ECIS technology, bioelectrical interface parameters such as the intercellular electrical resistance, the cell-substrate resistance and the cell-membrane capacitance can be recorded, which can be taken as indicators of cell migration and barrier function (Ebrahim et al., 2022). These electrical markers have also been used to track cell shape changes during apoptosis (Arndt et al., 2004). More advanced functionalities of ECIS have been demonstrated by integrating microfluidics into the platforms, allowing, for instance, tumor cell sorting from a blood sample (Burinaru et al., 2022).

Among all these developments, assays monitoring invasion processes are rare. The visualization and theoretical basis for such complex assays are still to be explored. The acquisition of temporal information during the cell invasion process has been accomplished with good reliability and feasibility by determining impedance value changes (Hong et al., 2011; Moghtaderi et al., 2024; Anchan et al., 2019). However, bioelectrical understanding and quantitative possibilities of this technique in probing multifactor interactions such as cell invasion dynamics remain challenging. Therefore, further studies are required to advance such assays beyond conventional adhesion and migration monitoring.

In the current work, we study invasion dynamics via ECIS utilizing our *in vitro* model of human embryo implantation. Changes of the phase information of the impedance spectra reflect differences between maternal endometrial epithelial monolayer formation and trophoblast invasion. We show that quantification of this process can be achieved by decomposing the ECIS spectra into individual resistance and capacitance parameters based on the respective cut-off frequencies. We can distinguish three stages of the invasion process in our assays, namely preinvasion, early-stage invasion and late-stage invasion.

We furthermore extend the conventional two-component ECIS theory to a three-component system consisting of the microelectrode, the endometrial monolayer and trophoblast spheroids. The establishment and further development of this technique will pave the way for future ECIS assays of cell invasion in different paradigms and pathological diagnosis in diverse multicellular interactions.

2. Materials and methods

2.1. ECIS chip cleaning

In this study, we employed an 8-well array ECIS chip integrated culture ware (8W1E, Applied BioPhysics, USA). Each well is integrated with an Au working electrode of 250 μm diameter opening, on a PET (polyethylene terephthalate, standard thickness 0.25 mm) passivated substrate for cell culture. The ECIS chips were cleaned with DI-water and sterilized with UV-light before usage. For reuse of the devices, the medium was aspirated from the chips using a vacuum pump, chips were incubated with 4% trypsin (500 μL, BD Biosciences, USA) at 37 °C and 5% CO_2, rinsed with DI-water, and sterilized under UV light for 1 h.

2.2. Endometrial monolayers

Cell-related operations were performed on a clean bench, inside class 2 cabinets Mars from Labogene (Denmark). Ishikawa cells (ECACC99040201; RRID: CVCL_2529), a well-differentiated human endometrial adenocarcinoma cell line, was used to form a monolayer on the gold (Au) ECIS electrodes (Nishida, 2002). Dulbecco's modified Eagle's medium/Ham's F12 (DMEM/F12, Product No. 11320033, Sigma-Aldrich, USA) was used as basal medium, supplemented with 10% (v/v) steroid hormone-free fetal calf serum (Product No. S-15-M, C. C.Pro, Germany), 2.5 mM L-glutamine (Product No. A2916801, Gibco, UK) and 1% v/v antibiotic-antimycotic (Product No. 12352207, Sigma-Aldrich, USA). Complete culture medium was used for the culturing of all cell types individually and during invasion co-culture experiments. The cells were seeded at a density of $1 \times 10^5/\text{cm}^2$ with 500 μL culture medium and cultured for at least 48 h to form a monolayer. The cell culture medium was changed every 48 h.

2.3. Trophoblast spheroids

Spheroids were generated using the AC-1M88 cell line (ACC457; RRID: CVCL_1803) (Gonzalez et al., 2011; Sternberg et al., 2024). For generation of spheroids, agarose micro-molds were produced in-house by pouring 3% agarose (Biozym Scientific GmbH, Hessisch Oldendorf, Germany) into 3D, 16×16 molds (MicroTissues Inc., Sigma-Aldrich, St. Louis, MO, USA). Then, AC-1M88 cell suspensions were placed in the agarose micro-molds at a concentration of 200 000 cells per mL of culture medium and grown in scaffold-free environment for 72 h before starting the experiments.

2.4. Attachment and invasion assays

Mature spheroids were placed on top of endometrial Ishikawa monolayer regions growing above electrodes. The EIS data collections were executed 6 h, 24 h, 30 h and 48 h after transferring the trophoblast spheroids on top of the Ishikawa monolayers (Fig. 1b, right). Since the spheroids were transferred manually, they were categorized based on the initial coverage of the electrode into high and low coverage groups. Spheroids typically attached to the surface of the endometrial monolayer and invaded it within 6 h. After seeding and during measurements, the cells and ECIS chips were placed inside a cell culture incubator that maintained 37 °C and 5% CO_2.

For the positive control group, 1.5 μM ethylene glycol tetraacetic acid (EGTA, Sigma-Aldrich, USA) was added to the medium to induce disassembly of cell-cell junctions, followed by two measurements after 6 and 24 h incubation. For the negative control group, the monolayer was treated with 4% trypsin (BD Biosciences, USA) to induce cell detachment, followed by a 20 min incubation before the measurements.

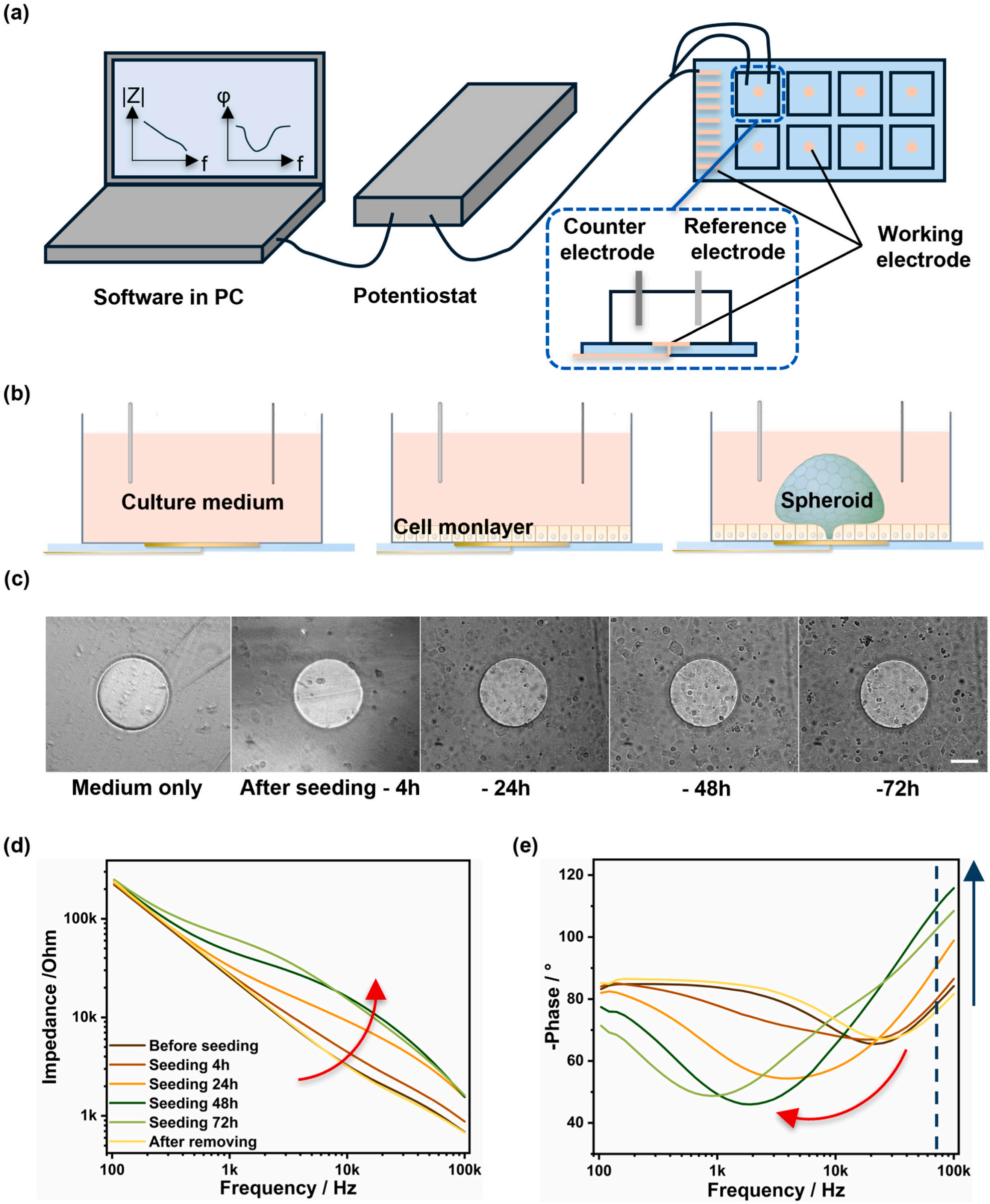

Fig. 1. Illustration of the ECIS setup for label-free cell dynamics monitoring: **(a)** Schematics of the potentiostat setup. The ECIS chip was connected via three electrodes (WE, CE and RE). Data was collected and plotted in the form of Nyquist or Bode plots. **(b)** Representative illustration of three cell-chip interacting conditions that were studied in this work: cell culture medium only, Ishikawa cell monolayer formation and trophoblast spheroid invasion. **(c)** Representative optical images of monolayer formation dynamics showing medium only, and 4 h, 24 h, 48 h, and 72 h after Ishikawa cell seeding. Scale bar: 100 μm. **(d, e)** Bode plot of impedance amplitude **(d)** and phase **(e)** during the Ishikawa monolayer formation process. The plot also shows the results after removal of the monolayer by 4% trypsin treatment.

2.5. Live-cell tracking

Ishikawa cells were grown for 3-5 days in standard conditions until they reached confluence. The Ishikawa monolayers were then confronted with the trophoblast spheroids. The trophoblast spheroids were pre-stained for 1 h with the live cell dye CellTracker Green (Thermo Fisher Scientific Inc., Waltham, USA) and Ishikawa cells were pre-stained for 1 h with live cell dye CellTracker Deep Red (Thermo Fisher Scientific Inc., Waltham, USA). The invasion of the individual AC-1M88 spheroids through the Ishikawa cell monolayer was monitored over a period of 48 h following the initial spheroid transfer. Spheroids were visualized at time points 8-12, 24 and 48 h. Images were obtained using a laser scanning confocal microscope (LSM710, Zeiss, Germany).

2.6. Label-free optical observation

An inverted optical microscope (Axio Observer, ZEISS, Germany) was used for visual observation of Ishikawa cells that were cultured as adherent monolayers at the bottom of the culture wells. Imaging was performed under sterile conditions. The 10×/0.25 Epiplan objective (ZEISS, Germany) was used.

2.7. Electrical impedance spectroscopy measurements

Electrical impedance spectroscopy was measured with the CompactStat2.h potentiostat (Ivium Technologies, the Netherlands) with integrated impedance analyser and operated through the accompanying IviumSoft software (Ivium Technologies, the Netherlands). Impedance spectra were measured from 100 Hz to 100 kHz in 46 distinct frequencies with a perturbation amplitude of 50 mV. A three-electrode setup was utilized: The Au microelectrode of the ECIS chip served as working electrode, a Platinum (Pt) wire as a counter electrode and an Ag/AgCl wire as the reference electrode. All electrodes and cables were secured with clips and locally separated to minimize measurement artifacts from electrical conductance. The EIS data of the monolayer formation were collected before seeding cells, and after 4 h, 24 h, 48 h and 72 h seeding, respectively.

The monitoring over time was performed in Bode plot, in which the impedance amplitude and phase were visualized. For further analysis, the impedance was divided into resistance and frequency-dependent capacitance. The division was under the contemplation that the whole system was treated as a resistance R_{sum} and capacitance C_{sum} in an in-series circuit (Urdapilleta et al., 2006). Nyquist plot was introduced in the modeling, where it shows the real and imaginary part of the impedance value.

2.8. Electrical equivalent circuit modeling

The electrode-electrolyte interface (cell culture medium) was modeled using the Randles equivalent circuit (Randles, 1947). Previous modelling of the ECIS has two branches, microscopic behaviour dominated, Giaever-Keese model (Giaever and Keese, 1991) and Lo-Giaever-Keese model (Lo et al., 1995), in which current flow was modeled on cell level; and macroscopic behaviour dominated, RC-parallel model (Wegener et al., 1996) and mean-field model (Urdapilleta et al., 2006), where object is the monolayer. Recently, the mesoscopic model (Buchini Labayen et al., 2022) was proposed.

Based on previews applications (Jiang et al., 2024; Kauth et al., 2024), this work is extending the classical EEC model to characterize two distinct phases during spheroid invasion. To analyze the data, we separated the active invasion phase into early-stage invasion and late-stage invasion. Additional spheroid resistance ($R_{spheroid}$) and capacitance ($C_{spheroid}$) were added to the invasion circuit model. An open-source software EIS spectrum analyser (Bondarenko et al., 2005) was used for data fitting. The fittings were executed using the Powell algorithm, which performed 2000 iterations. Resulting Nyquist and Bode plots of the impedance data shown in this publication compare experimental data and model fits. In our invasion assays, depending on the initial coverage, the time point for sensing could vary. Only in the high coverage case, we modeled the data with the EEC to understand the invasion dynamics.

2.9. Data processing and statistical analysis

The Bode plot, resistance and capacitance in dependence of frequency were plotted in Origin Pro 2024 (OriginLab, USA). For resistance spectra, we applied a first-order differentiation to identify the transition frequency marking the boundary between low- and high-frequency regimes.

All analyzed data represent three independent biological replicates, each with three technical repetitions. Triplicate measurements were performed for each sample at every timepoint. Quantitative data are expressed as mean ± standard deviation (SD). Statistical significance was calculated via the Tukey algorithm with independent biological repetitions ($N = 3$). Significant difference values were presented in $p < 0.05$ *, $p < 0.005$ ** and $p < 0.001$ ***.

2.10. ZO-1 immunofluorescence staining

ZO-1 immunofluorescence staining was performed to evaluate junctional organization of Ishikawa endometrial cell monolayers during AC-1M88 trophoblast spheroid invasion. For visualization of invasion, trophoblast spheroids were pre-stained with CellTracker Green (Thermo Fisher Scientific Inc., Waltham, USA). Co-cultures were fixed at 6 h, 24 h, 30 h, and 48 h following spheroid placement using methanol for 2 min, followed by acetone for 20 s at room temperature. After fixation, co-cultures were washed 3 times with PBS, then, samples were blocked with 3% bovine serum albumin (BSA; Sigma-Aldrich, St.Louis, MO,USA) for 1 h at room temperature.

Co-cultures were incubated overnight at 4 °C with ZO-1 polyclonal antibody (2.5 μg/mL in 1% BSA; Product No. 40-2200, Invitrogen, USA). After washing, samples were incubated with donkey anti-rabbit IgG (H + L), DyLight®550-conjugated secondary antibody (Product No. DkxRb-003-F550NHSX, ImmunoReagents, USA) for 1 h at room temperature. Nuclei were counterstained with Hoechst 33342 (1 μg/mL) for 15 min, and samples were mounted using Elvanol mounting medium.

Images were acquired using a Zeiss Axio Observer 7 microscope (Zeiss, Germany) under identical acquisition settings for all time points.

2.11. Apoptosis detection assay

Apoptosis was assessed using the NucView 488 Caspase-3 Assay Kit (30029, Biotium, USA). Co-culture samples were incubated with 5 μM caspase-3 substrate solution in complete culture medium for 30 min prior to fixation. After incubation, samples were fixed with 4% paraformaldehyde (PFA; Carl Roth, Karlsruhe, Germany) for 15 min. After washing 3 times, samples were mounted with Elvanol mounting medium. Images were acquired using a Zeiss Axio Observer 7 microscope (Zeiss, Germany) under identical acquisition settings for time points 24 h, 30 h and 48 h. Representative images are shown in Fig. S1.

3. Results and discussion

3.1. ECIS monitoring of endometrial Ishikawa cell monolayer formation

Endometrial Ishikawa cell monolayer formation was dynamically monitored over 72 h via ECIS using standard Au microelectrodes (250 μm in diameter) with optical control of cell morphology and viability (Fig. 1a–c). An overall increase in impedance was detected in the ECIS spectrum 48 h after cell seeding. During this period phase spectra shifted to lower frequencies approaching a phase of 0° (Fig. 1d–e). Afterwards, stabilized impedance was recorded with overlapping spectra from 6 to 100 kHz and slightly increased impedance amplitudes between 300 Hz and 6 kHz (Fig. 1d). These changes can be taken as evidence for the formation of a confluent monolayer after two days, when cells had formed tight junctions (Wegener, 2019) (Fig. 1c).

To prove that the impedance changes are due to monolayer formation, cells were detached by trypsin after 72 h. As expected, both the impedance and phase spectra returned to the initial baseline status (Fig. 1d–e). The relevance of junction-mediated monolayer formation for cell impedance was further validated by EGTA treatment. This chelator reduces calcium concentration and thereby disrupts calcium-dependent cell-cell junctions (Rothen-Rutishauser et al., 2002) (positive control, Fig. S2). As a negative control impedance measurements were also performed for a 4% trypsin solution only (Fig. S3). Table S1 presents a comparative overview of the impedance values acquired at 10 kHz and 100 kHz subsequent to the different experimental treatments.

3.2. *ECIS monitoring of trophoblast spheroid invasion*

In the next set of experiments, trophoblast spheroids of comparable size (200 - 300 μm diameter) were placed on the confluent Ishikawa cell monolayers. To investigate the sensing resolution of the ECIS method in the invasion process, two different initial spheroid-to-electrode coverage conditions were defined for low coverage (17 ± 3%) and high coverage (65 ± 4%) (Fig. 2). As shown in Fig. 2a and c the invasion process was optically tracked (blue dashed circles) in relation to the Au working electrodes (red dashed circles; 250 μm diameter), which corresponds to the effective sensing area of each chip. Independent of the initial seeding position, the eventual flattening area of the spheroid often exceeded the working electrode area over time due to trophoblast cell migration and displacement of Ishikawa cells.

Increase in impedance was consistently observed 24 h after spheroid placement (Fig. 2b and d). During this time, the Ishikawa cell monolayer was still present between the spheroid and the electrode, getting gradually replaced by penetrating and migrating spheroid-derived trophoblast cells. Notably, decreasing spheroid-electrode coverage correlated with longer time intervals to reach the maximum impedance spectra values (from 24 h up to 30-48 h). This may be due to the fact that it took longer for the slightly off-site spheroids to cover the entire electrode with outgrowing cells.

Two distinct peaks were observed in the phase spectra 6 h after seeding (depicted in violet in Fig. 2b and d), located at low frequency (∼1 kHz) and high frequency (∼40 kHz), respectively. Since the resistance biased peak at 1k Hz was not observed in the Ishikawa monolayer only (Fig. 1), we conclude that it is caused by the attachment of the spheroid. The subsequent disappearance after 24 h indicates that the spheroid has merged into the cell monolayer. The remaining high frequency peak shifted gradually towards lower frequencies after 24 h, suggesting the full integration of the spheroid into the endometrial Ishikawa monolayer.

To test whether the changes in impedance correlate with different stages of trophoblast-endometrium interaction, microscopic analyses were performed. In the first set of experiments, trophoblast spheroids were pre-stained with CellTracker Green, nuclei were stained with Hoechst 33343 and tight junctions were labeled with antibodies against ZO-1. The images in Fig. 2e show that characteristic tight junction strands are maintained throughout the invasion process not only within the endometrial Ishikawa monolayer and AC-1M88 spheroids but also between both. The anti-ZO-1 labeling became even more pronounced over time. In the next set of experiments, AC-1M88 and Ishikawa cells and were separately labelled with different CellTracker dyes to monitor the progression of trophoblast invasion relative to the endometrial monolayer. Fig. 2f presents details how spheroid-derived cells attach to the endometrial monolayer (4 h), penetrate it (8 h, 24 h) and eventually displace it (24 h, 48 h). The process is coupled to flattening of the spheroid during intraepithelial expansion. To exclude that increased apoptosis of the endometrial epithelium contributes to trophoblast invasion and expansion, we tested for caspase-3 activity. Fig. S1 shows that apoptotic cells are not localized at the invasion front.

Taken together, the microscopic analyses in combination with the ECIS measurements lead to the conclusions that the transient resistive phase peak at low frequencies (∼1 kHz) can be taken as an indicator of spheroid attachment, that its disappearance is a consequence of trophoblast invasion and that the shift of the high frequency peak to lower frequencies correlates with trophoblast integration into the endometrial monolayer.

3.3. *Analysis of trophoblast spheroid invasion*

Cell-impedance analysis is strongly associated with cell growth at the cell-electrode interface, which induces changes in resistance and capacitance. These electrical changes are related to cell-substrate adhesion, cell-cell contacts and cell morphology. To delineate the frequency-dependent contribution of these parameters in our invasion assays, the cut-off frequency separating low- and high-frequency regimes of the spectra was calculated (Table S2 and Fig. 3a). We selected for this cut-off the point of maximal first-order derivative of the resistance, indicating a sharp transition in resistive behavior. Generally, such a transition is characteristics of RC parallel circuits, where the current flow in the low-frequency range is primarily governed by the resistor, which is an indicator for evaluating cell proliferation, tight junction formation and barrier function in previous work, while the capacitive reactance increases markedly with decreasing frequency (Equation (1)).

$$Z_C = 1/j\omega C \tag{1}$$

Where Z_C is the capacitive reactance, j is the imaginary unit, $\omega = 2\pi f$ is the angular frequency and f is the frequency and C is the capacitance. In contrast, at the high-frequency regime, the reactance of the capacitor decreases substantially, causing current to flow predominantly through the capacitive pathway, i.e., the cell membrane, making capacitance particularly informative for assessing membrane integrity and dielectric properties (Wegener et al., 2000; Engel et al., 2023; Bounik et al., 2022).

The cut-off frequencies that represent the transition to the high-frequency regime are presented in Fig. 3a. As expected, the frequencies shifted over time with increased variation due to the heterogeneous nature of the biological invasion process. Such a phenomenon is also visible in the phase spectra as depicted in Fig. 1e and 2b, d (blue dashed lines), respectively. The overall cut-off frequencies during 24 h invasion were statistically determined as follows: 54.7 ± 8.3 kHz for high coverage, 81.6 ± 26.0 kHz for low coverage and 63.3 ± 0.0 kHz for the monolayer, which is the frequency point that significant resistance transition occurred (Table S2).

Impedance quantification could also be obtained at a fixed frequency (Fig. 2). For example, in high coverage case, the impedance amplitude increased from ∼1.9 kΩ (monolayer) to ∼4 kΩ at 6 h and to ∼8 kΩ at 24 h, followed by a plateau between 30 and 48 h (∼6 kΩ) at the 54.7 kHz cut-off frequency (Fig. 2b). In the same cut-off frequency, the phase of the impedance shifted accordingly from −50° (monolayer) to −74° after 6 h of spheroid attachment, and further to −88° after 24 h, when the invasion process was almost completed. This progressive increase in the capacitive reactance reflects the flattening of the spheroid and its interaction with the Ishikawa cell layer (red arrow in the phase of the impedance). After 30 h, the phase recovered and capacitively stabilized at −79°, suggesting the termination of the invasion process with successful replacement of the initial Ishikawa monolayer on the microelectrodes (Fig. 2f).

A similar trend was also observed in the low spheroid coverage experiments (Fig. 2d), where the capacitive characteristics at cut-off frequency (81.6 kHz) increased from −62° (6 h) to −77° (24 h), towards −90° after 30 h. Compared with high coverage group, stabilization of the impedance value in low coverage group required more time due to

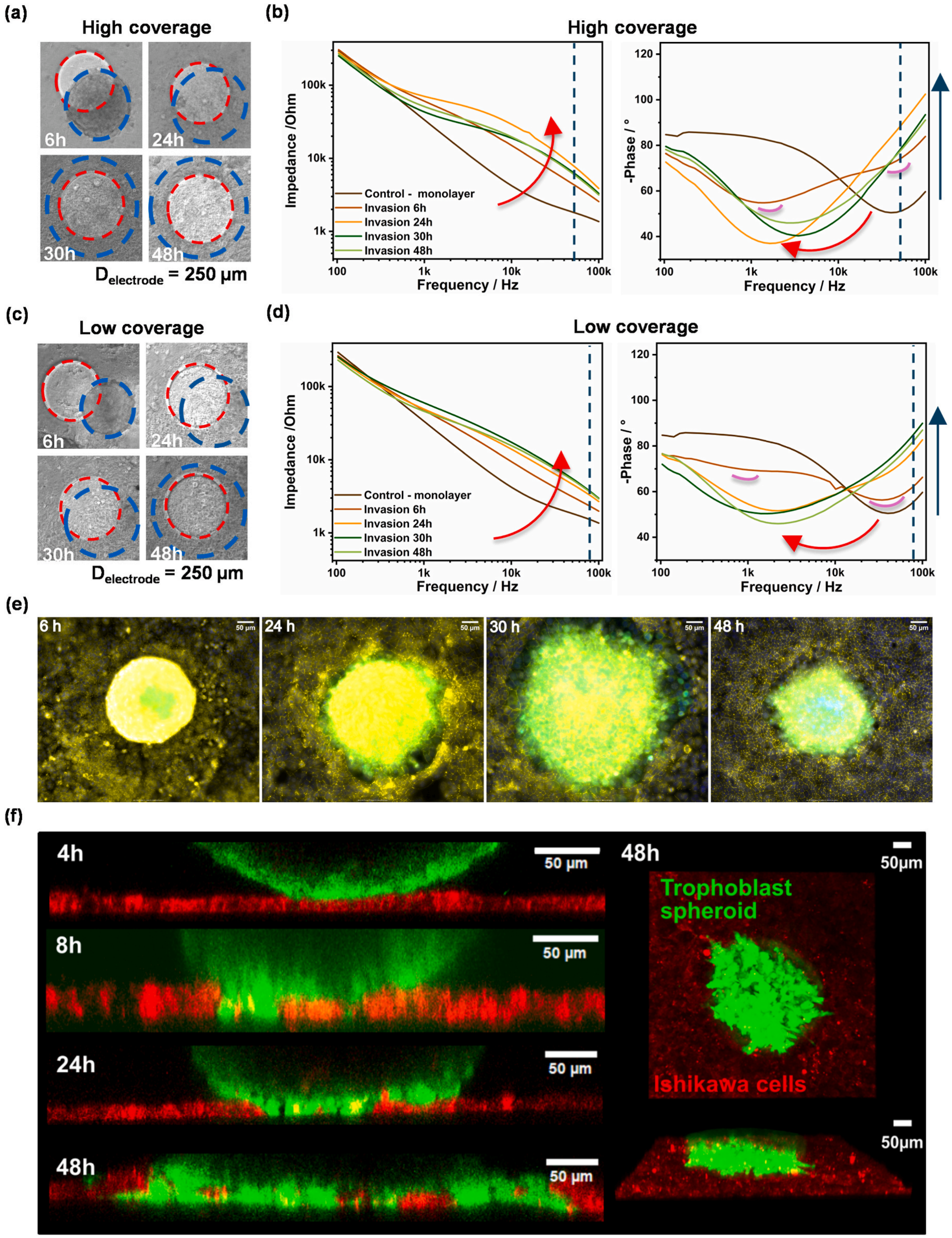

Fig. 2. Microscopic observations and Bode plots of invasion over time in various initial spheroid coverages of the electrode. Optical observation and Bode plot of **(a–b)** high coverage and **(c–d)** low coverage, respectively. The blue dotted vertical lines in the phase spectra **(b)**, **(d)** indicate the cut-off frequencies. Complete data are presented in Table S2. **(e)** Representative immunofluorescence images showing ZO-1 (yellow) localization in Ishikawa cell monolayers during trophoblast spheroid invasion at time points 6 h, 24 h, 30 h, and 48 h(left to right). Trophoblast spheroids were pre-stained with CellTracker Green (CTG; green), and nuclei were counterstained with Hoechst 33342 (blue). **(f)** Representative images of trophoblast spheroid attachment and invasion stages at different time points. The left micrographs present the z-projections of the invasion sites at the timepoints 4-48 h. The right micrograph presents the basal plane of the invasion site (upper) and the same 3D image as a tilted whole plane (lower) at the timepoint 48 h. Trophoblast cells (spheroid) were pre-stained with the live cell dye CellTracker Green (CTG) and Ishikawa cells were pre-stained with the live cell dye CellTracker Deep Red (CTDR).

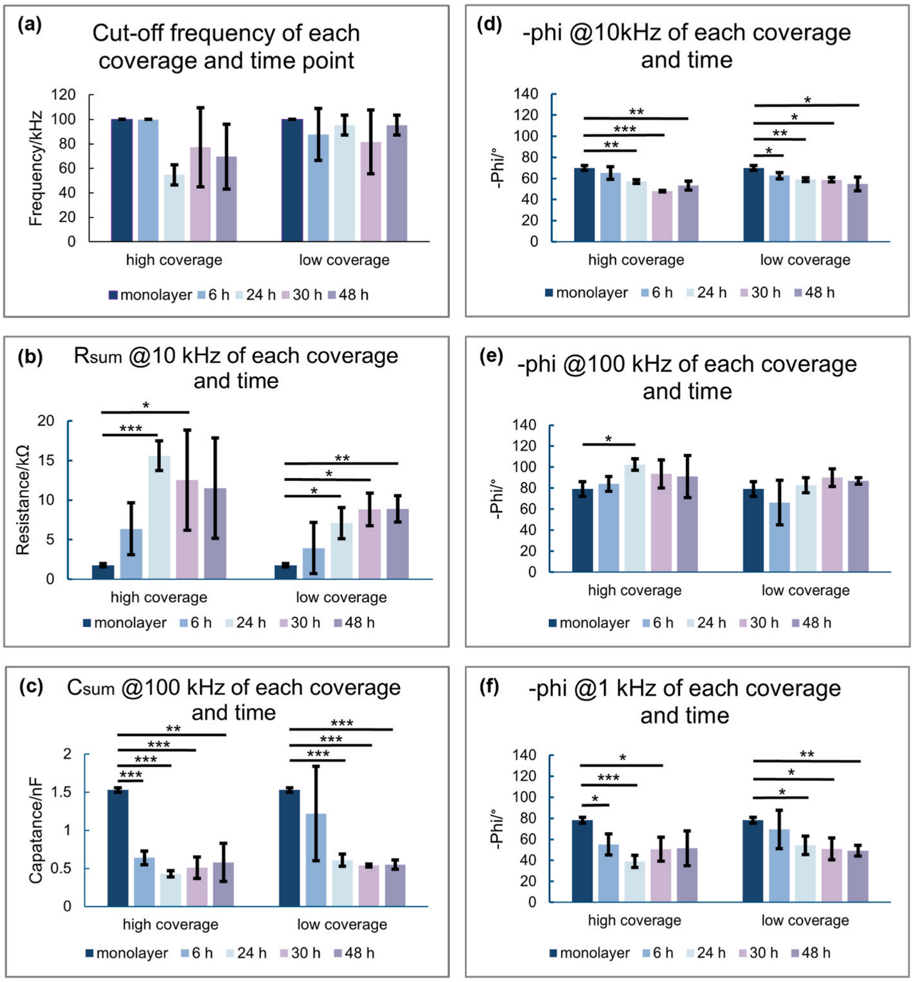

Fig. 3. Quantitative impedimetric analysis for the invasion monitoring assays: **(a)** The cut-off frequencies from resistive to capacitive behavior over various coverage areas and time points. The frequency values are presented, where the largest first-order derivatives of measured resistance values were found; Value of R **(b)** and C **(c)** at a low frequency (10 kHz) and high frequency (100 kHz) point. Value of phase at 10 kHz **(d)**, 100 kHz **(e)** and 1 kHz **(f)**. Numerical data is available in the supporting information, Table S3, S4 and S5. Statistical significance values were presented in $p < 0.05$ *, $p < 0.005$ ** and $p < 0.001$ ***.

different effective sensing areas, confirming the importance of spheroid-electrode positioning for invasion monitoring.

Within the cut-off frequency range, the resistance exhibited a sharp transition, making it difficult to fully resolve the resistive and capacitive behaviors (Fig. S4 and S5). Based on this, the low frequency 10 kHz regime and the 100 kHz high frequency regime were selected to study frequency-dependent variations in resistance, capacitance and phase at different time points of the invasion process to provide a useful metric for cell-electrode interactions (Fig. S4 and S5). Additionally, the phase at 1 kHz, which was captured in early invasion stage was studied (Fig. 3b–f).

At 10 kHz, a significant increase in R_{sum} was observed for all progression stages of the invasion processes, consistent with a significant visibility in the phase values of the impedance (Fig. 3b and d, Fig. S6b). For instance, R_{sum} increased from 1.77 kΩ to 6.37 kΩ after 6 h, and reached a maximum of 15.60 kΩ after 24 h in the high coverage situation. It was followed by a slight drop and later stabilization around 12 kΩ (Fig. 3b). This phenomenon reflects the process during which the spheroid attaches to the monolayer (6 h) and subsequently invades it (24 h) until a new monolayer is established (30-48 h). This dynamic process is reflected in a strong variation of the impedance phase between -47.9° and -65.2° (Fig. 3d).

In contrast, a significant decrease in C_{sum} was recorded at 100 kHz during invasion, with a relatively stable phase around -90°, showing a dominating capacitive behavior (Fig. 3c and e, Fig. S6a). For instance, in the high coverage condition, C_{sum} displays a decrement from 1.53 nF to 0.74 nF until 24 h, followed by a subsequent increment to 1.07 nF after 30 h and stabilization at ~1 nF after 48 h. Furthermore, a pure capacitive phase could be observed ~ -90° after 30 h (Fig. 3e), corresponding to the reconstruction of a new monolayer after successful invasion.

This supports our assays of using the cut-off frequency to distinguish the low- and high-frequency regions for resistive and capacitive quantification. Additionally, the quantification of phase at 1 kHz, at which the resistive phase peak occurred at early invasion stage, demonstrated similar trend to the quantification statistics at 10 kHz (Fig. 3f). This implies the potential of using phase as a sensitive indicator for invasion process monitoring at low frequency range.

At high frequency ranges, certain phase measurements exceeded the theoretical limit (-90°) for ideal RC circuits. This phenomenon may result from non-ideal capacitive behavior, including parasitic inductances or parallel parasitic capacitances introduced by non-ideal resistors within the complex measurement setup.

3.4. EEC modelling of spheroid-monolayer invasion dynamics

To provide better explanation of the dual-peak phenomenon that was observed in the phase plots of the impedance during invasion, as well as the quantified resistance and capacitance, we introduced a representative three-component EEC considering the electrode, endometrial monolayer and trophoblast spheroid (Fig. 4). Both the monolayer and

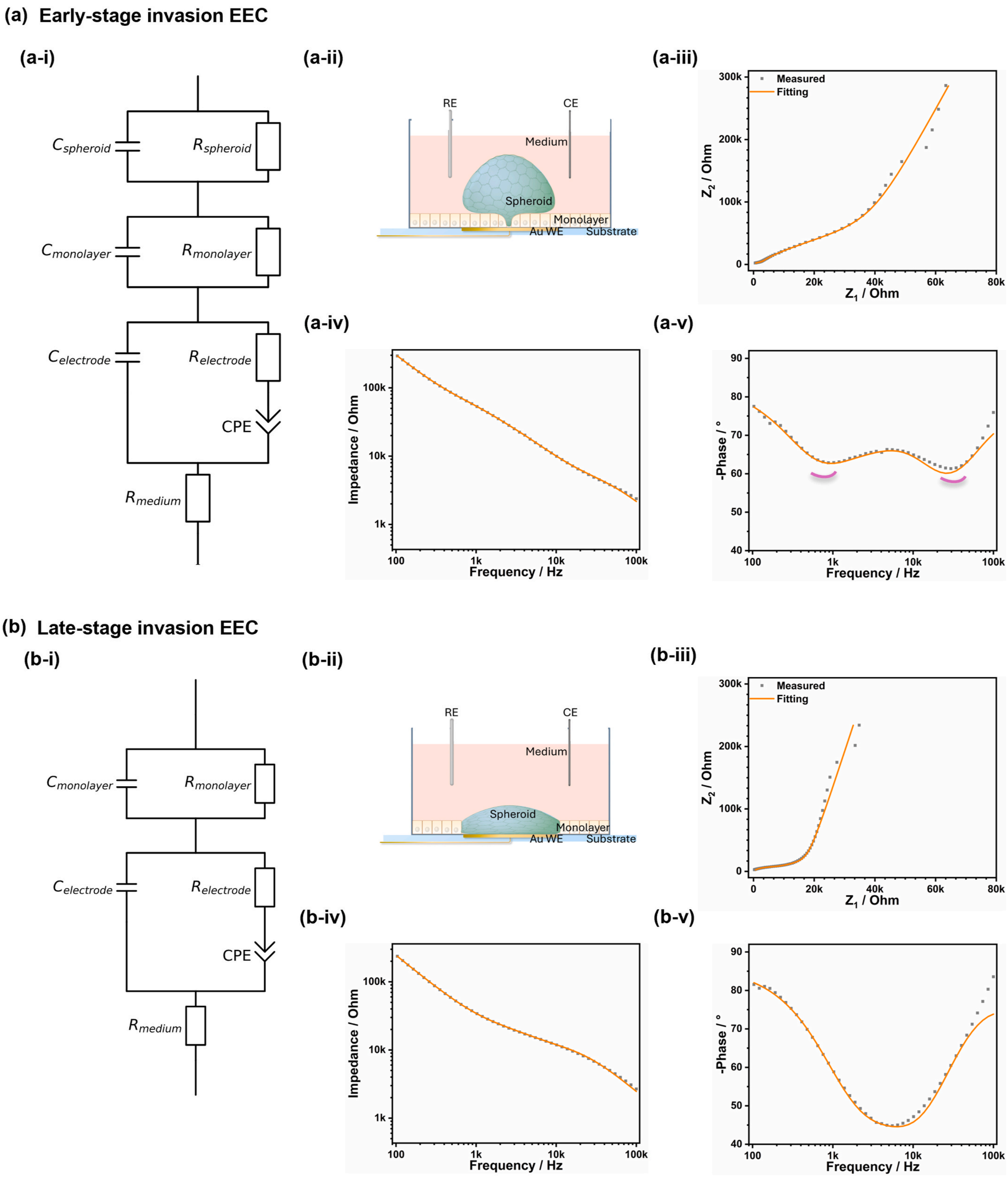

Fig. 4. EEC models and the fitting results of spheroid early-stage invasion **(a)** and late-stage invasion **(b)**. **(i)** EEC model; **(ii)** sideview of the cell culture well; **(iii-v)** Impedance fitting in Nyquist plot; **(iii),** impedance **(iv)** and phase **(v)** spectrum of either early-stage or late-stage invasion, respectively.

the spheroid conditions were modeled as parallel RC circuits consisting of a resistor and a capacitor, in accordance with established RC circuit concepts (Susloparova et al., 2015; Wegener, 2019; Wegener et al., 1996).

The EEC models were constructed based on the proposed invasion status as illustrated in Fig. 4, Fig. S7 and S8. All fittings exhibited n-values of the typically used constant-phase element (CPE, Equation (2), in which Q_0 is a constant and n is between 0 and 1. If $n = 0$, Z_{CPE} is a resistance; if $n = 1$, Z_{CPE} is a capacitance) approaching 1 (0.94), indicating a nearly ideal capacitive behavior at the microelectrode interface (Table S6). However, it dropped to 0.89 in the early-stage invasion model. This suggests an interfacial complexity and disorder, consistent with the assumption that the structural integrity of the monolayer becomes nonuniform during invasion. The subsequent rise to 0.93 in the late-invasion stage model indicates a recovery of the structural organization, reflecting the formation of a new quasi-monolayer state.

$$Z_{CPE} = \frac{1}{Q_0(j\omega)^n} \tag{2}$$

In all cases, the overall EEC fitting from 100 Hz to 100 kHz was in line with the experimental results (Nyquist and Bode plots, Fig. 4 iii-v). Although slight scattering was observed at low frequency and high frequency fitting due to the surface heterogeneity of Au electrodes (Kauth et al., 2024) and non-ideal capacitive behavior (Fig. 3) (Barsoukov and Ross Macdonald, 2018), respectively. Notably, the double peak in the phase plot that occurred after 6 h invasion (Fig. 2) was also successfully demonstrated in the circuit fitting, validating its function as sensitive electric marker to determine early-stage invasion.

The resistance (R_{sum}) and capacitance (C_{sum}) values were calculated for all EEC models according to Equation (3), where $|Z|$ and φ are impedance and phase value from the Bode plot, respectively. Specifically, 10 kHz and 100 kHz were selected to represent the low and the high frequency regime to compare with experimental results in Table 1 and Table S7. As shown in the monolayer modelling, an increase of $R_{sum,fit}$ from 1.32 kΩ (medium) to 5.50 kΩ (monolayer) was obtained at 10 kHz. In the meantime, the $C_{sum,fit}$ decreases from 2.42 nF (medium) to 1.06 nF (monolayer) at 100 kHz. In the invasion modeling, from early-stage to late-stage invasion, an increase of $R_{sum,fit}$ from 4.30 kΩ to 8.31 kΩ was observed at 10 kHz, and a decrease of $C_{sum,fit}$ from 0.78 nF to 0.67 nF at 100 kHz was recorded. The fitting results align with experimentally proposed steps including the monolayer formation, spheroid attachment and invasion.

In addition, the experimental phase value measured above the cut-off frequency increases from partly resistive (~-60°) to pure capacitive behavior over time. This indicates the capacitive dominance at the high frequency regime during the invasion process, when the monolayer is replaced by the spheroid. In agreement with experimental characterization, the capacitive change at the low frequency regime (*e.g.* 10 kHz) were observed with large variations (Fig. S6b), limiting its function for biological quantification.

$$R = |Z|\cos\varphi, \qquad C = \left|\frac{1}{\omega|Z|\sin\varphi}\right| \tag{3}$$

4. Conclusion

This work provides a more detailed understanding of the frequency-dependent correlation between cell-impedance and cellular invasive behavior, defining quantitative electrical markers for characterization of invasion process.

As an electric marker, the peak observed in the phase plot at ~1 kHz allowed a clear distinction between the monolayer formation and the early-stage spheroid invasion. During the late-stage invasion a significant increase in resistive dominance was observed at low frequency together with a significant drop in the capacitive path over time until the invasion was completed. This frequency-dependent information can be used to quantify the invasion process. Furthermore, variations in spheroid–electrode positioning, which determine the initial electrode coverage area, significantly affect impedimetric signal stabilization.

By decomposing the impedance spectrum into resistance and capacitance, we introduced the concept of cut-off frequency to distinguish between low- and high-frequency domains during cell growth and invasion. The resistance (R_{sum}) and capacitance (C_{sum}) both below (*e.g.* 10 kHz) and above cut-off frequencies (*e.g.* 100 kHz) were quantitively analyzed. Their changes aligned with the impedance amplitude and respective phase shifts during the monolayer formation and spheroid invasion. We suggest quantification of the system resistance and capacitance as low and high frequency markers to allow frequency-dependent quantification of cell-chip and spheroid-cell-chip interactions.

Table 1

R_{sum} and C_{sum} comparison between fitting and experimental results of early- and late-stage invasion.

Early-Invasion	$R_{sum,fit}$/kΩ	$R_{sum,exp}$/kΩ	|Error|/%	$C_{sum,fit}$/nF	$C_{sum,exp}$/nF	|Error|/%
@10 kHz	4.30	4.21	2.14 %	1.75	1.75	0
@100 kHz	0.73	0.58	25.86 %	0.78	0.69	13.04 %
Late-Invasion	$R_{sum,fit}$/kΩ	$R_{sum,exp}$/kΩ	|Error|/%	$C_{sum,fit}$/nF	$C_{sum,exp}$/nF	|Error|/%
@10 kHz	8.31	8.05	3.23 %	1.84	1.81	1.66 %
@100 kHz	0.69	0.3	130.00 %	0.67	0.60	11.67

Building upon established cell-substrate interface theories and previous monolayer EEC models, we extended the conventional EEC model to a three-component system, that accurately describes both the early-stage invasion and late-stage invasion dynamics at a broad frequency range (100 Hz to ~100 kHz). In agreement with experimental results, a complex phase spectrum with double peaks was observed, which can serve as an indicator of spheroid attachment at the early-stage invasion. In summary, a multi-step invasion process was proposed: 1) preinvasion - non-contact condition of the spheroidal trophoblast with the endometrial monolayer, 2) early-stage invasion (0-6 h) - trophoblast attachment and endometrial penetration, and 3) late-stage invasion (6-48 h) - spheroid flattening and expansion within the endometrial monolayer.

Our results advance the possibility of cell-electrical quantification to monitor biological processes which involve cell and tissue intercalation. Future work will focus on refining the invasion model by continuous data collection to identify intermediate invasion stages more precisely and incorporating additional circuit elements to represent multicellular structures through time-resolved, longitudinal impedance monitoring of living cultures throughout the invasion process. With a deeper understanding of frequency-dependent impedimetric signals, precise and spatially defined *in vitro* read out technologies will be developed in the future.

CRediT authorship contribution statement

Dongyang Tang: Data curation, Formal analysis, Investigation, Methodology, Validation, Visualization, Writing – original draft. **Liubov Izmaylova:** Data curation, Formal analysis, Methodology, Validation, Writing – review & editing. **Anil Can:** Methodology, Validation. **Sven Ingebrandt:** Resources, Supervision, Writing – review & editing. **Rudolf E. Leube:** Conceptualization, Funding acquisition, Resources, Supervision, Writing – review & editing. **Ziyu Gao:** Conceptualization, Funding acquisition, Project administration, Resources, Supervision, Writing – review & editing.

Declaration of competing interest

The authors declare that they have no known competing financial interests or personal relationships that could have appeared to influence the work reported in this article. This manuscript has not been published previously and is not under consideration for publication elsewhere. All authors have approved the final version of the manuscript and consent to its submission to *Biosensors and Bioelectronics: X*. We declare no conflicts of interest.

Acknowledgements

Authors thank Ms. Sarah Göbbels for technical support in biological experiments. Authors thank the Deutsche Forschungsgemeinschaft (DFG) for funding (363055819/GRK2415). It was also funded by the Federal Ministry of Education and Research (BMBF) and the Ministry of Culture and Science of the German State of North Rhine-Westphalia (MKW) under the Excellence Strategy of the Federal Government and the Länder (ERS-OPSF906).

Appendix A. Supplementary data

Supplementary data to this article can be found online at https://doi.org/10.1016/j.biosx.2026.100797.

Data availability

Data will be made available on request.

References

Agilent, 2025. xCELLigence real-time cell analysis. https://www.agilent.com/en/product/cell-analysis/real-time-cell-analysis.

Anchan, A., Kalogirou-Baldwin, P., Johnson, R., Kho, D.T., Joseph, W., Hucklesby, J., Finlay, G.J., O'Carroll, S.J., Angel, C.E., Graham, E.S., 2019. Real-time measurement of melanoma cell-mediated human brain endothelial barrier disruption using electric cell-substrate impedance sensing technology. Biosensors (Basel) 9.

Applied BioPhysics, Inc, 2025. ECIS® Z-Theta 16 or 96 well array station. https://www.biophysics.com/ztheta.php.

Arndt, S., Seebach, J., Psathaki, K., Galla, H.J., Wegener, J., 2004. Bioelectrical impedance assay to monitor changes in cell shape during apoptosis. Biosens. Bioelectron. 19, 583–594.

Barsoukov, Evgenij, Ross Macdonald, J., 2018. Impedance Spectroscopy.

Bentin-Ley, U., Horn, T., Sjogren, A., Sorensen, S., Falck Larsen, J., Hamberger, L., 2000. Ultrastructure of human blastocyst-endometrial interactions in vitro. J. Reprod. Fertil. 120, 337–350.

Bondarenko, A.S., Ragoisha, G.A., Pomerantsev, A.L., 2005. Progress in chemometrics research. Nova Science 89–102.

Bounik, R., Cardes, F., Ulusan, H., Modena, M.M., Hierlemann, A., 2022. Impedance imaging of cells and tissues: design and applications. BME Front. 2022, 1–21.

Buchini Labayen, A.C., Bellotti, M.I., Bast, W., Bonetto, F.J., 2022. Electrical cell impedance spectral mesoscopic model applied to experimental data of variable size microelectrodes. Phys. Rev. E 105, 044401.

Burinaru, Tiberiu A., Adiaconiţă, Bianca, Avram, Marioara, Preda, Petruţa, Enciu, Ana-Maria, Chiriac, Eugen, Mărculescu, Cătălin, Constantin, Tiberiu, Militaru, Manuella, 2022. Electrochemical impedance spectroscopy based microfluidic biosensor for the detection of circulating tumor cells. Mater. Today Commun. 32.

Classen-Linke, I., Buck, V.U., Sternberg, A.K., Kohlen, M., Izmaylova, L., Leube, R.E., 2025. Changes in epithelial cell polarity and adhesion guide human endometrial receptivity: how in vitro systems help to untangle mechanistic details. Biomolecules 15.

Ebrahim, Abdul Shukkur, Ebrahim, Thanzeela, Hussein, Kani, Ahmed, S Ibrahim, Carion, Thomas W., Berger, Elizabeth A., 2022. Functional optimization of electric cell-substrate impedance sensing (ECIS) using human corneal epithelial cells. Sci. Rep. 12, 14126.

Engel, N., Dau, M., Engel, V., Franz, D., Klemmstein, F., Thanisch, C., Kolb, J.F., Frank, M., Springer, A., Kohling, R., Bader, R., Frerich, B., Wiesmann, N., Heimes, D., Kammerer, P.W., 2023. Combining electrostimulation with impedance sensing to promote and track osteogenesis within a titanium implant. Biomedicines 11.

Fang, Y., Jingjing, F., Tiantain, C., Huanhuan, X., Qiaohua, H., 2023. 'Impact of the number of previous embryo implantation failures on IVF/ICSI-ET pregnancy outcomes in patients younger than 40 years: a retrospective cohort study'. Front Endocrinol (Lausanne) 14, 1243402.

Franks, W., Schenker, I., Schmutz, P., Hierlemann, A., 2005. 'Impedance characterization and modeling of electrodes for biomedical applications'. IEEE Trans. Biomed. Eng. 52, 1295–1302.

Gauster, M., Moser, G., Wernitznig, S., Kupper, N., Huppertz, B., 2022. Early human trophoblast development: from morphology to function. Cell. Mol. Life Sci. 79, 345.

Giaever, Ivar, Keese, Charles R., 1984. Monitoring fibroblast behavior in tissue culture with an applied electric field. Proc. Natl. Acad. Sci. 81, 3761–3764.

Giaever, I., Keese, C.R., 1991. Micromotion of Mammalian Cells Measured Electrically, vol. 88. Proceedings of the National Academy of Sciences, pp. 7896–7900.

Gonzalez, Marina, Neufeld, Julia, Reimann, Katja, Wittmann, Stefanie, Samalecos, Annemarie, Wolf, Anja, Bamberger, Ana-Maria, Gellersen, Birgit, 2011. Expansion of human trophoblastic spheroids is promoted by decidualized endometrial stromal cells and enhanced by heparin-binding epidermal growth factor-like growth factor and interleukin-1β. Mol. Hum. Reprod. 17, 421–433.

Hazelgrove, Brittany, Matter, Lukas, Raos, Brad, Harland, Bruce, Cheng, Leo, Asplund, Maria, Darren, Svirskis, 2025. Electrochemical impedance spectroscopy in vivo for neurotechnology and bioelectronics. Nat. Rev. Electr. Eng. 2, 110–124.

Hong, J., Kandasamy, K., Marimuthu, M., Choi, C.S., Kim, S., 2011. 'Electrical cell-substrate impedance sensing as a non-invasive tool for cancer cell study'. Analyst 136, 237–245.

Jiang, Huijie, Gao, Ziyu, Lubrano, Claudia, Bovio, Claudia Latte, Bommes, Henning, Kauth, Andrea, Baumann, Lea, Cheng, Bo, Murugan, Divagar, Knoch, Joachim, Waser, Rainer, Ingebrandt, Sven, Santoro, Francesca, Pachauri, Vivek, 2024. Metal-organic frameworks as an active substrate for cell-interaction studies and cell-on-a-chip platforms. Biosens. Bioelectron. X 19.

Kauth, Andrea, Wegener, Joachim, Jiang, Huijie, Pachauri, Vivek, Ingebrandt, Sven, 2024. PEDOT:PSS electropolymerization protocol for microelectrodes enabling low-cost impedance-based cellular assays. Appl. Res.

Kok, R.N.U., Spoelstra, W.K., Betjes, M.A., Van, J.S., Tans, S.J., 2025. 'Label-free cell imaging and tracking in 3D organoids'. Cell Rep. Phys. Sci. 6.

Lo, C.M., Keese, C.R., Giaever, I., 1995. 'Impedance analysis of MDCK cells measured by electric cell-substrate impedance sensing'. Biophys. J. 69, 2800–2807.

Magar, H.S., Hassan, R.Y.A., Mulchandani, A., 2021. Electrochemical impedance spectroscopy (EIS): principles, construction, and biosensing applications. Sensors (Basel) 21.

Mao, X., Zhang, J., Chen, Q., Kuang, Y., Zhang, S., 2017. Short-term copper intrauterine device placement improves the implantation and pregnancy rates in women with repeated implantation failure. Fertil. Steril. 108, 55–61 e1.

Moghtaderi, Hassan, Sadeghian, Golfam, Abiri, Hamed, Khan, Faizullah, Rahman, Md Mizanur, Ahmed, Al-Harrasi, Rahman, Shaikh Mizanoor, 2024. Electric cell-substrate impedance sensing in cancer research: an in-depth exploration of impedance sensing for profiling cancer cell behavior. Sens. Acutators Rep. 7.

Nishida, M., 2002. The Ishikawa cells from birth to the present. Hum. Cell 15, 104–117.

Randles, John Edward Brough, 1947. Kinetics of rapid electrode reactions. Discuss. Faraday Soc. 1, 11–19.

Rothen-Rutishauser, B., Riesen, F.K., Braun, A., Günthert, M., Wunderli-Allenspach, H., 2002. Dynamics of tight and adherens junctions under EGTA treatment. J. Membr. Biol. 188, 151–162.

Ruane, P.T., Garner, T., Parsons, L., Babbington, P.A., Wangsaputra, I., Kimber, S.J., Stevens, A., Westwood, M., Brison, D.R., Aplin, J.D., 2022. 'Trophectoderm differentiation to invasive syncytiotrophoblast is promoted by endometrial epithelial cells during human embryo implantation'. Hum. Reprod. 37, 777–792.

Sternberg, A.K., Izmaylova, L., Buck, V.U., Classen-Linke, I., Leube, R.E., 2024. An assessment of the mechanophysical and hormonal impact on human endometrial epithelium mechanics and receptivity. Int. J. Mol. Sci. 25.

Susloparova, A., Koppenhofer, D., Law, J.K., Vu, X.T., Ingebrandt, S., 2015. 'Electrical cell-substrate impedance sensing with field-effect transistors is able to unravel cellular adhesion and detachment processes on a single cell level'. Lab Chip 15, 668–679.

Urdapilleta, E., Bellotti, M., Bonetto, F.J., 2006. 'Impedance analysis of cultured cells: a mean-field electrical response model for electric cell-substrate impedance sensing technique'. Phys. Rev. E - Stat. Nonlinear Soft Matter Phys. 74, 041908.

Wegener, Joachim, 2019. Label-Free Monitoring of Cells in Vitro. Springer, Cham.

Wegener, J., Keese, C.R., Giaever, I., 2000. 'Electric cell-substrate impedance sensing (ECIS) as a noninvasive means to monitor the kinetics of cell spreading to artificial surfaces'. Exp. Cell Res. 259, 158–166.

Wegener, J., Sieber, M., Galla, H.J., 1996. 'Impedance analysis of epithelial and endothelial cell monolayers cultured on gold surfaces'. J. Biochem. Biophys. Methods 32, 151–170.

Wissmann, R., Martirosian, P., Danalache, M., Grozinger, G., Schick, F., Elser, S., 2025. Imaging cell spheroid clusters: an MRI protocol for non-invasive standardized characterization. Heliyon 11, e41803.

Supplementary information

Time-resolved monitoring and circuit modeling of trophoblast invasion in a model of human embryo implantation by electric cell-substrate impedance sensing

Dongyang Tang[a], Liubov Lzmaylova[b], Anil Can[b], Sven Ingebrandt[a], Rudolf E. Leube[b], Ziyu Gao[a,*]

[a] Institute of Materials in Electrical Engineering 1, RWTH Aachen University, 52074 Aachen, Germany.

[b] Institute of Molecular and Cellular Anatomy, RWTH Aachen University, D-52074 Aachen, Germany.

* Corresponding author: Dr. Ziyu Gao, Email: ziyu.gao@iwe1.rwth-aachen.de

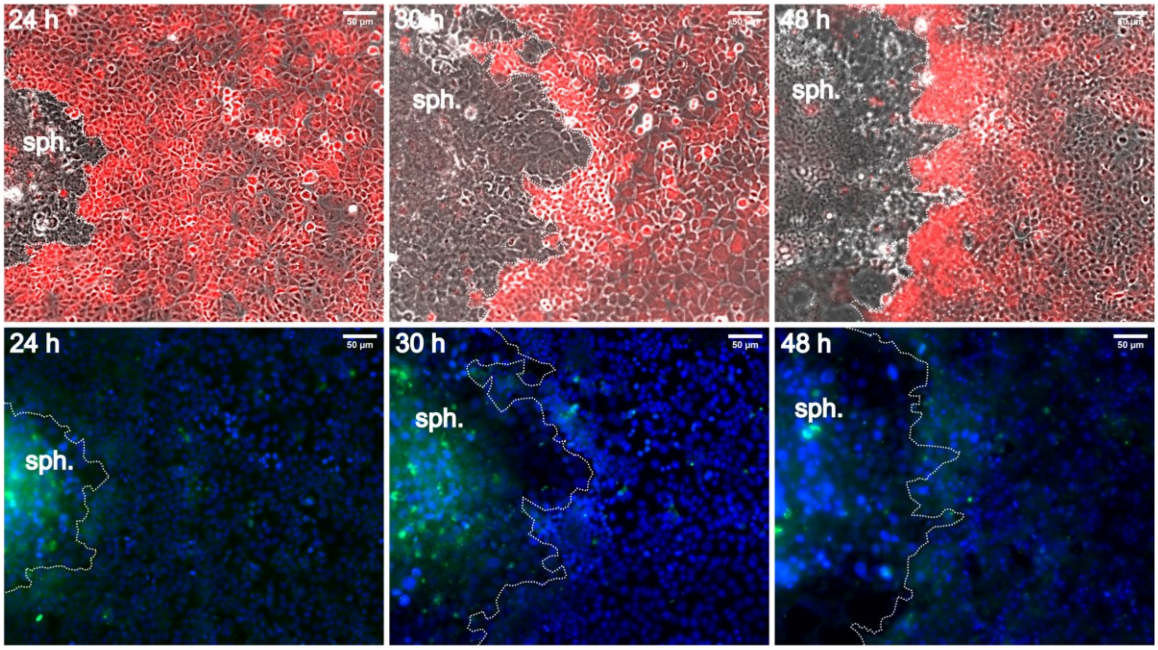

Figure S1. Representative images showing apoptosis during AC-1M88 trophoblast spheroid (sph.) invasion at time points 24 h, 30 h, and 48 h (left to right). The first row shows phase-contrast images illustrating spheroid invasion into the Ishikawa monolayer, pre-stained with CellTracker Deep Red (red). The second row displays corresponding merged fluorescence images showing caspase-3 activity (green), indicating apoptotic cells in both trophoblast spheroids and the Ishikawa monolayer. Nuclei were counterstained with Hoechst 33342 (blue). Apoptotic cells are not accumulated in the invasion front, which is marked with dotted white line, but rather localized to the middle of the spheroid.

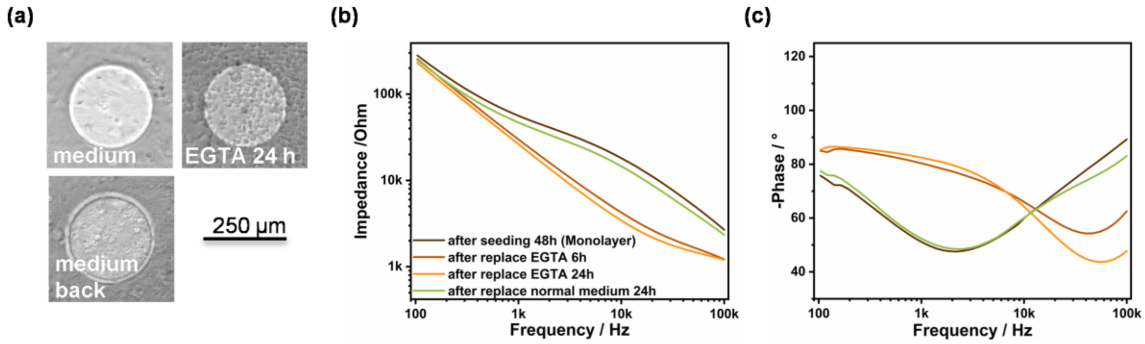

Figure S2. Positive control for junction-dependance of impedance measurements. **(a)** Shows microscopic phase contrast images of the Ishikawa cells growing on the circular electrodes before, after 24 hours of EGTA treatment and after another switch to normal medium for 24 hours. **(b-c)** Presents corresponding Boden plots.

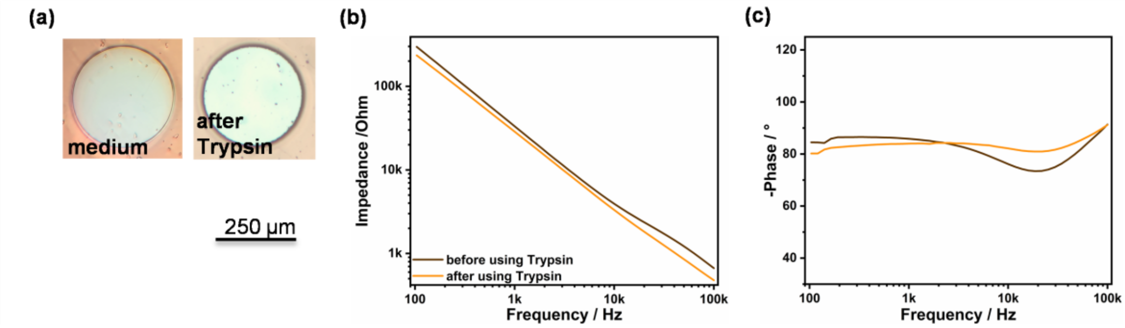

Figure S3. Negative control for cell-dependence of impedance measurements. 4% trypsin was added to the cell culture medium for 15 min to detach and dissociate the Ishikawa cell monolayer **(a)** optical microscopic images of the electrode after removing the culture medium and after removing 4% Trypsin. **(b-c)** corresponding Boden plot.

(a) **High coverage**

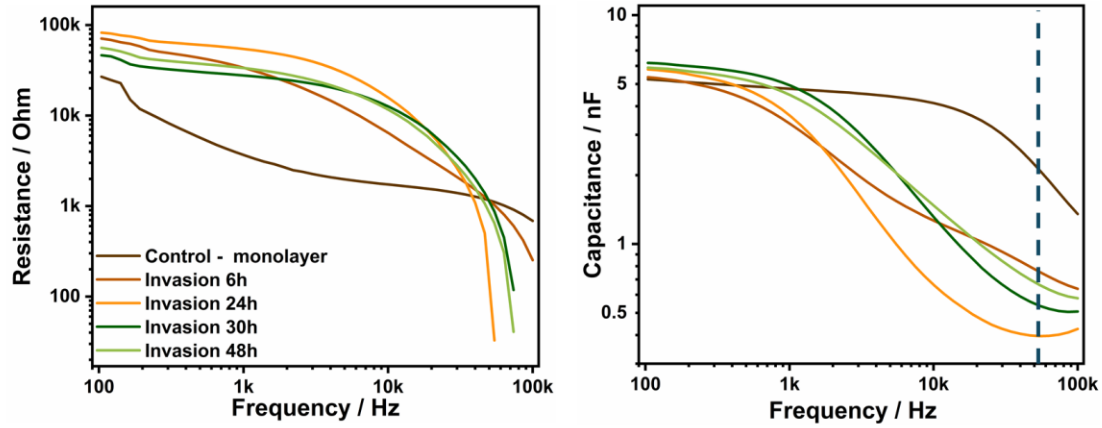

(b) **Low coverage**

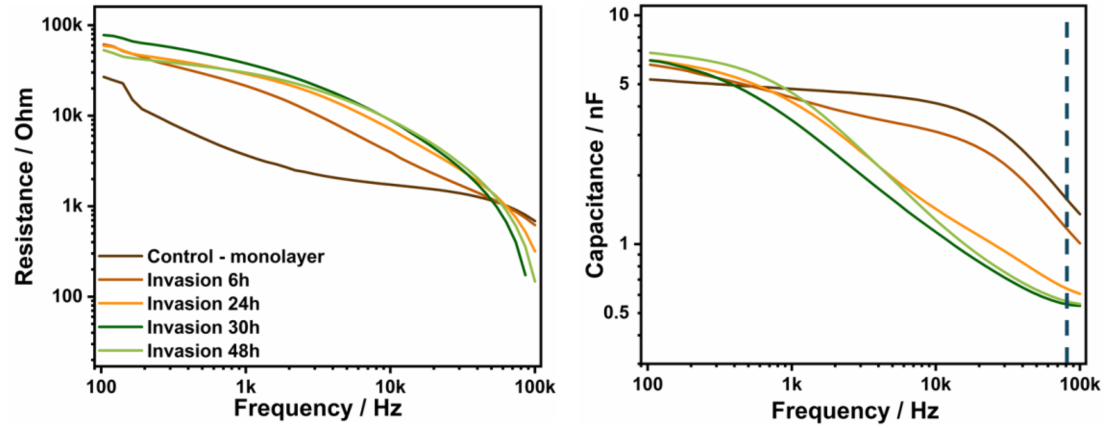

Figure S4. Resistance R_{sum} (left) and capacitance C_{sum} (right) measurements at different frequencies (100 Hz to 100 kHz) of Ishikawa cell monolayers after 6 hours, 24 hours, 30 hours and 48 hours of placing trophoblast spheroids covering the Au electrodes by high (**a**), and low **(b)** coverage.

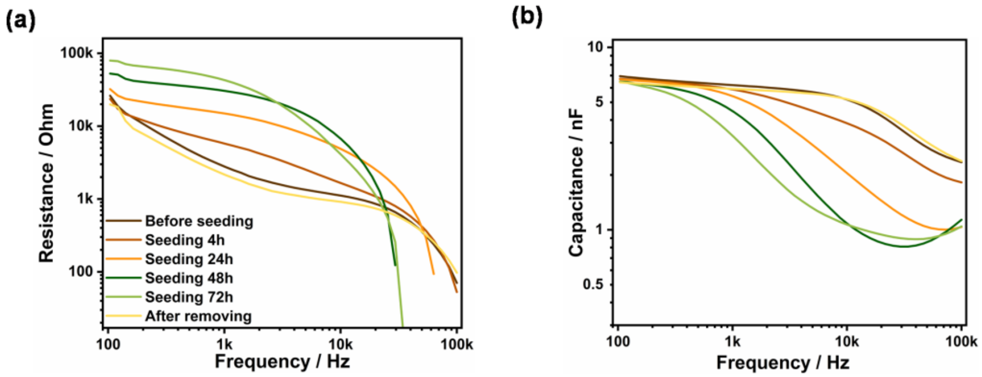

Figure S5. (a) Resistance R_{sum} and **(b)** capacitance C_{sum} measurements at stimulation frequencies between 100 Hz and 100 kHz of Ishikawa monolayers and after different times of placing trophoblast spheroids and after their removal of the monolayer by 4% trypsin treatment.

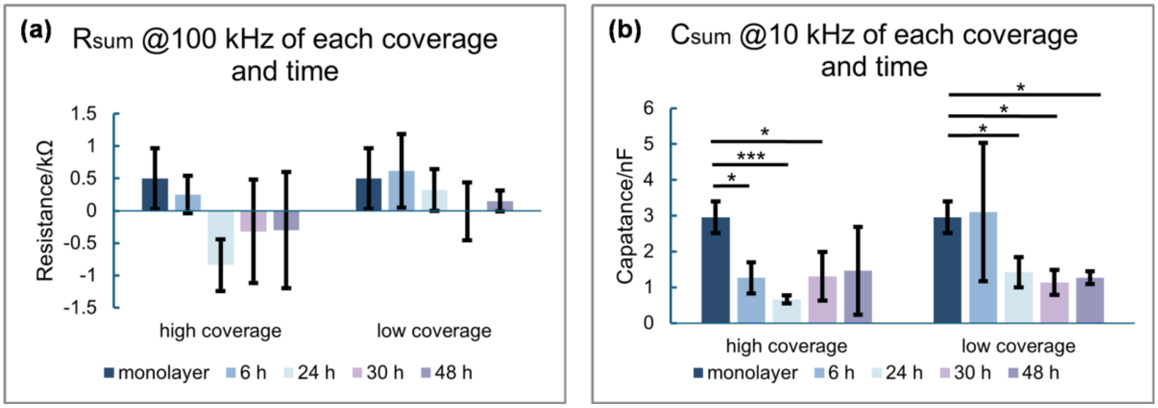

Figure S6. **(a)** Resistance R_{sum} at high frequency (100 kHz) and **(b)** capacitance C_{sum} at low frequency (10 kHz) measured in Ishikawa cell monolayers after placing trophoblast spheroids with different degrees of coverage of the Au electrode.

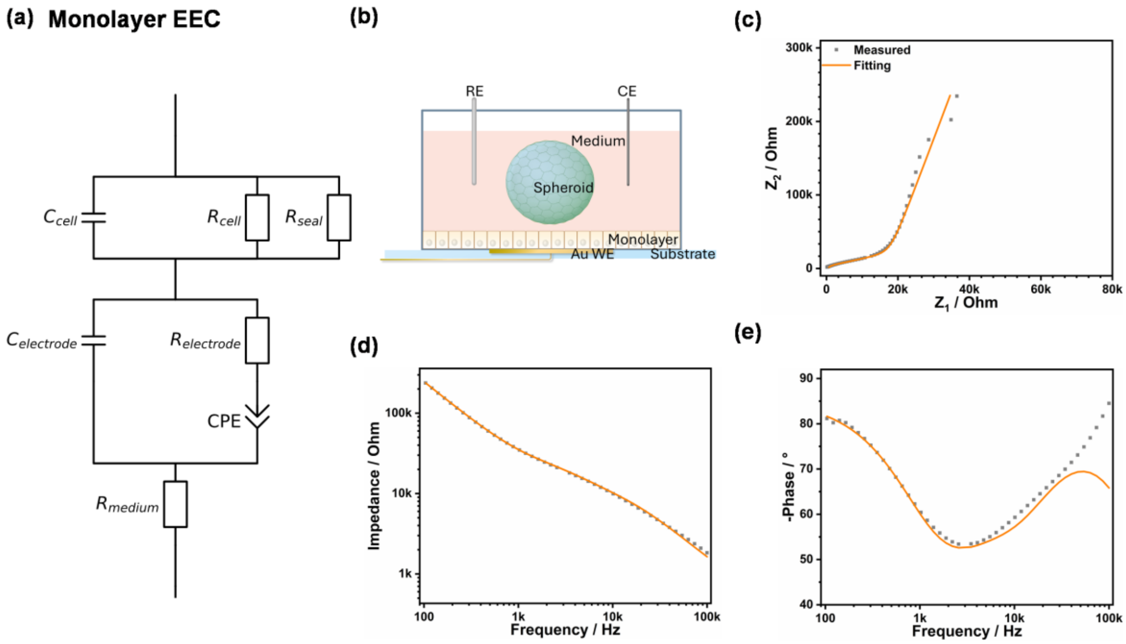

Figure S7. Equivalent electrical circuit (EEC) models and the fitting results of medium. **(a)** EEC; **(b)** Schematic representation of the experimental setup with non-attached trophoblast spheroid floating in the medium above the confluent endometrial monolayer; **(c-e)** Graphs of impedance fitting as Nyquist plot **(c)**, impedance measurements **(d)** and phase spectrum **(e)**.

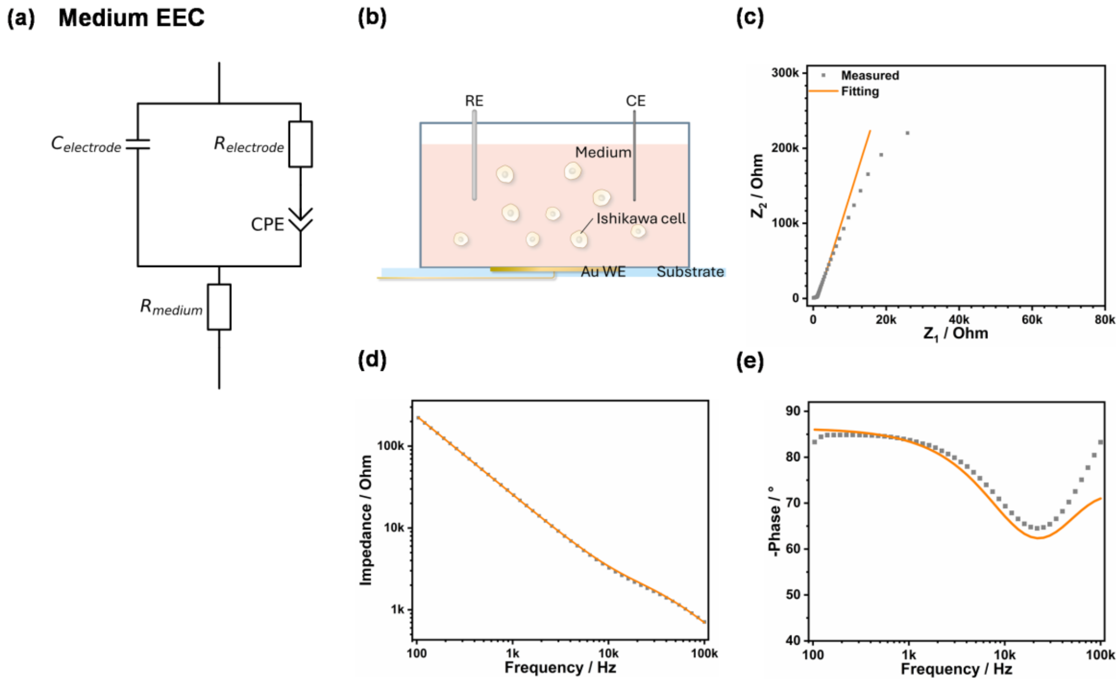

Figure S8. Equivalent electrical circuit (EEC) models and the fitting results of dissociated Ishikawa cells. **(a)** EEC; **(b)** Schematic illustration of the experimental setup consisting of the Au working electrode (Au WE). **(c-e)** show graphs of the impedance fitting as a Nyquist plot **(c)**, impedance measurements **(d)** and phase spectrum **(e)**.

Table S 1. The table shows values of impedance at 10 kHz and 100 kHz for different operations.

Impedance / kΩ	@ 10 kHz	@ 100 kHz
Medium only	25.14±0.46	3.24±0.12
Seeding after 48h	55.41±0.32	18.00±0.06
EGTA medium after 24h	25.60±0.30	3.40±0.07
Changing back to normal medium	46.33±2.54	14.47±0.50
Removing cells with 4% Trypsin	26.27±0.02	3.16±0.01

Table S 2. The table shows the cut-off frequencies determined for Ishikawa monolayers before and after spheroids seeding with low and high spheroid-electrodes coverage conditions (calculated from area that spheroid covered to electrode area in 6 hours). The frequency values shown correspond to the largest first-order derivatives of the measured resistance values.

Frequency /kHz	**6 h**	**24 h**	**30 h**	**48 h**	**Note: Coverage ratio**
Monolayer	100.0 ± 0.0 (4h)	63.3 ± 0.0	N/A	92.2 ± 15.2	N/A
High coverage	100.0 ± 0.0	54.7 ± 8.3	77.2 ± 32.3	69.6 ± 26.4	65±4%
Low coverage	87.8 ± 21.2	95.3 ± 8.2	81.6 ± 26.0	95.3 ± 8.2	17±3%

Table S 3. The table shows the values of resistance (R) and capacitance (C) measured at a low frequency (10 kHz) and high frequency (100 kHz) in Ishikawa cell monolayers before and at different time points after placing trophoblast spheroids covering the Au electrodes to different coverage.

Time point		**monolayer**	**6 h**	**24 h**	**30 h**	**48 h**
R/kΩ @10 kHz	High coverage	1.77±0.21	6.37±3.29	15.6±1.88	12.52±6.34	11.52±6.36
	Low coverage	1.77±0.21	3.93±3.23	7.08±1.97	8.82±2.08	8.89±1.65
C/nF @100 kHz	High coverage	1.53±0.03	0.64±0.09	0.43±0.04	0.51±0.14	0.58±0.25
	Low coverage	1.53±0.03	1.22±0.62	0.61±0.08	0.54±0.02	0.55±0.06

Table S 4. The table shows the values of resistance (R) and capacitance (C) measured at a low frequency (100 kHz) and high frequency (10 kHz) in Ishikawa cell monolayers before and at different time points after placing trophoblast spheroids covering the Au electrodes to different coverage.

Time point		**monolayer**	**6 h**	**24 h**	**30 h**	**48 h**
R/kΩ @100 kHz	High coverage	0.50±0.47	0.25±0.29	-0.84±0.40	-0.32±0.80	-0.30±0.90
	Low coverage	0.50±0.47	0.62±0.57	0.32±0.32	-0.01±0.45	0.15±0.16
C/nF @10 kHz	High coverage	2.96±0.44	1.26±0.43	0.66±0.11	1.30±0.68	1.46±1.23
	Low coverage	2.96±0.44	3.10±1.93	1.42±0.42	1.14±0.35	1.27±0.18

Table S 5. Value of -phi at a low frequency (1 kHz and 10 kHz) and high frequency (100 kHz). The table shows the values of -phi determined for a low frequency (1 kHz and 10 kHz) and high frequency (100 kHz) stimulation of Ishikawa cell monolayers before and at different time points after placing trophoblast spheroids covering the Au electrodes to different coverage.

Time point		**monolayer**	**6 h**	**24 h**	**30 h**	**48 h**
-Phi/° @10 kHz	High coverage	70.0±2.2	65.2±6.0	57.2±1.8	47.9±0.7	53.1±4.3
	Low coverage	70.0±2.2	62.7±2.9	58.8±1.8	58.7±2.1	54.7±6.5
-Phi/° @100 kHz	High coverage	79.1±7.0	84.0±7.0	102.5±5.3	93.5±13.3	91.1±20.0
	Low coverage	79.1±7.0	66.3±21.3	82.7±7.2	89.9±8.5	87.0±3.2
-Phi/° @1 kHz	High coverage	78.2±2.8	55.2±10.0	39.1±5.9	50.6±11.6	51.5±16.5
	Low coverage	78.2±2.8	69.5±18.2	54.4±8.8	51.0±10.5	49.2±5.1

Table S6. The table lists EEC fitting data of the proposed spheroid cell invasion process in comparison to medium alone.

Parameter	**Medium (error %)**	**Monolayer (error %)**	**Early invasion (error %)**	**Late invasion (error %)**
$C_{electrode}$/nF	2.24 (11.55%)	1.33 (9.56%)	2.38 (3.10%)	2.76 (4.41%)
C_{cell}/nF	/	4.63 (22.44%)	/	/
$C_{monolayer}$/nF	/	/	7.14 (8.60%)	0.85 (5.51%)
$C_{spheroid}$/nF	/	/	1.14 (7.60%)	/
R_{medium}/Ω	91 (9.58%)	250 (23.87%)	180 (24.08%)	280 (15.81%)
$R_{electrode}$/Ω	3198 (6.69%)	10000 (16.90%)	34793 (13.65%)	27950 (13.41%)
R_{cell}/Ω	/	10297 (23.80%)	/	/
R_{seal}/Ω	/	280 (22.66%)	/	/
$R_{monolayer}$/Ω	/	/	3020 (6.16%)	8546 (4.98%)
$R_{spheroid}$/Ω	/	/	21943 (12.61%)	/
CPE/$_{nFs^{(n-1)}}$	6.77 (3.28%)	7.64 (8.13%)	6.40 (5.38%)	5.96 (5.90%)
n	0.94 (0.38%)	0.94 (1.02%)	0.89 (0.76%)	0.93 (0.78%)

Table S7. R_{sum} and C_{sum} comparisons between fitting and experimental results of both medium and monolayer cases

Medium	**$R_{sum,fit}$ / kΩ**	**$R_{sum,exp}$ / kΩ**	**|Error| / %**	**$C_{sum,fit}$ / nF**	**$C_{sum,exp}$ / nF**	**|Error| / %**
@10 kHz	1.32	1.15	14.78 %	5.05	5.17	2.3 %
@100 kHz	0.23	0.08	187.50 %	2.42	2.26	7.08 %

Monolayer	**$R_{sum,fit}$ / kΩ**	**$R_{sum,exp}$ / kΩ**	**|Error| / %**	**$C_{sum,fit}$ / nF**	**$C_{sum,exp}$ / nF**	**|Error| / %**
@10 kHz	5.50	5.07	8.48 %	1.84	1.84	0
@100 kHz	0.67	0.18	272.22 %	1.06	0.87	21.83 %